AIII and BDI Topological Systems at Strong Disorder

Juntao Song[1,2] and Emil Prodan[1]
[1]*Department of Physics, Yeshiva University, New York, NY 10016, USA*
[2]*Department of Physics, Hebei Normal University, Hebei 050024, China*

Using an explicit 1-dimensional model, we give a direct evidence that the 1-dimensional topological phases from the AIII and BDI symmetry classes follow a $\mathbb{Z}$-classification, even in the strong disorder regime when the Fermi level is embedded in dense localized spectrum. The main tool for our analysis is the winding number ν, in the non-commutative formulation introduced in Ref. [1]. For both classes, by varying the parameters of the model and/or the disorder strength, a cascade of sharp topological transitions $\nu = 0 \to \nu = 1 \to \nu = 2$ is generated, in the regime where the insulating gap is completely filled with localized spectrum. We demonstrate that each topological transition is accompanied by an Anderson localization-delocalization transition. Furthermore, to explicitly rule out a $\mathbb{Z}_2$ classification, a topological transition between $\nu = 0$ and $\nu = 2$ is generated. These two phases are also found to be separated by an Anderson localization-delocalization transition, hence proving their distinct identity.

PACS numbers: 03.65.Vf, 05.30.Rt, 71.55.Jv, 73.21.Hb

arXiv:1402.7116v1 [cond-mat.dis-nn] 28 Feb 2014

I. INTRODUCTION

The topological phases from the AIII and BDI symmetry classes are classified by the winding number ν of the ground state. The classification table of topological insulators and superconductors [2, 3] predicts that non-trivial topological phases exist in the AIII symmetry class for each odd space-dimension. Furthermore, in each odd space-dimension, it is predicted that there are as many topological phases as integer numbers are in the additive $\mathbb{Z}$ group. For the BDI symmetry class, the table predicts a very different scenario. Here, topological phases appear in 0 and 1 space-dimensions, after which there is a void and the next space-dimension where non-trivial topological phases exist is 5. In some dimensions, such as 0, 7 and 8, the classification is $\mathbb{Z}_2$, while for other dimensions, such as 1 and 11, the classification is $\mathbb{Z}$. In dimension 5, the classification is $2\mathbb{Z}$. It has been argued [2], based on the nonlinear-sigma-model, that this classification remains valid in the regime of strong disorder. This regime, however, is extremely difficult to analyze theoretically because the quantum states cross the Fermi level both from above and below upon deformations of the models, making any argument based on a tiny insulating gap invalid. As always, it is desirable to have a direct confirmation of these predictions, and this is one of our goals for the present work. We focus exclusively on the 1-dimensional phases from the AIII and BDI symmetry classes, both predicted to obey a $\mathbb{Z}$-classification.

An explicit confirmation of the $\mathbb{Z}$ classification at strong disorder is especially important for the following reason. As shown in Ref. [1], there is an important relation between the winding number ν and the electric polarization P [4–9], whenever a chiral symmetry is present (which is the case for both AIII and BDI classes). The later is defined only by modulo integers, and due to the chiral symmetry, it can only take the values 0 and $\frac{1}{2}$. The relation between the two is:

$$P = 1/2\ (\nu \bmod 2). \tag{1}$$

This brings up a set of interesting and important questions. Since the electric polarization is one of the possible physical manifestations of the topological character, and this physical observable takes only two stable values, then: 1) Is ν itself taking only two stable values (0 and 1)? 2) If ν takes more than two stable values, is it true that all the corresponding topological phases are macroscopically distinct? For example, if ν is relevant only modulo 2, then the phase $\nu = 2$ would be trivial and we could cross between $\nu = 2$ to $\nu = 0$ phases without going throughout a quantum transition.

To conclusively demonstrate the $\mathbb{Z}$-classification, and entirely eliminate the possibility of a $\mathbb{Z}_2$-classification, we generate strongly disorder models which display topological phases with $\nu = 0$, 1 and 2, and study the cascade of topological transitions: $\nu = 2 \to \nu = 1 \to \nu = 0$. Sharp change of the quantized ν is observed at the phase boundaries, accompanied by an Anderson localization-delocalization transition. This shows that indeed the phases $\nu = 0$ and $\nu = 2$ are topologically distinct from the phase with $\nu = 1$. If the classification was by ν mod 2, then the phases $\nu = 0$ and $\nu = 2$ will be indistinguishable. To show that this is not the case, we searched in the parameter space for a situation where the phase $\nu = 0$ is in direct contact with the phase $\nu = 2$. After turning on the strong disorder, we similarly find an Anderson localization-delocalization phase transition along the entire phase boundary, proving that $\nu = 0$ and $\nu = 2$ are indeed distinct phases.

Another important issue is the characterization of these topological phases at strong disorder. It has been a widespread belief among our community that the topological invariants are carried by bulk extended states which resist the Anderson localization, and which reside at energies below and above the Fermi level. This characteristic has been indeed observed numerically for several symmetry classes [10–15]. However, the recent study [1] on the AIII symmetry class revealed that, in this particular case, the entire energy spectrum becomes localized as soon as the disorder is turned on, and stays

localized until an Anderson localization-delocalization transition builds up (from this entirely localized spectrum!) while crossing from a topological phase to another. One implication is that the winding number is *not carried* by extended states, and instead each localized state carries a small part of it. Another implication is that the divergence of the localization length doesn't have to happen through the levitation and annihilation of some extended states above and below the Fermi energy (as it always happen in classes A and AII [10, 11, 16]), and instead the divergence can develop from an entirely localized spectrum. Ref. [1] made the prediction that this uncharacteristic behavior is present in all symmetry classes where the E is fixed by the symmetry to a given value. The present work demonstrates that this is indeed true for the BDI class of topological insulators.

II. THE NON-COMMUTATIVE WINDING NUMBER: DEFINITION, CHARACTERIZATION AND COMPUTATION

The main tool in our analysis is the recently introduced non-commutative winding number ν [1], obtained by a real-space reformulation of the k-space expression, followed by a proper generalization to the disorder case. This invariant has been already demonstrated to remain quantized and non-fluctuating (from one disorder configuration to another), tough only in the $\nu = 1$ topological phase in the AIII symmetry class. The non-commutative formula of the winding number has the following attributes:

- It is well defined in the regime of strong disorder; All operations involved in the calculation make straightforward sense, as opposed to, for example, the twisted boundary conditions method where derivatives against the twist angles are invoked, but the multitude of states crossing the Fermi level destroy the required differentiability.
- It is self-averaging in the sense that its actual value can be determined from a single disorder configuration, provided the size of the simulation box is large enough.
- It can be evaluated numerically with extreme accuracy and efficiency [17]. In the present simulations, the quantization of the non-commutative winding number is exact up to at least six digits of precision.
- It can be rigorously characterized using Non-Commutative Geometry and shown to stay quantized and non-fluctuating as long as the Fermi level, which is fixed at $E = 0$, resides in a region of localized spectrum [18].

In the following we review the theory of the winding number in arbitrary odd space-dimension D, and present in more detail the numerical algorithm used to compute the non-commutative winding number.

A. Periodic Lattice Models with Chiral-Symmetry

The generic translational-invariant, multi-band lattice Hamiltonians take the form:

$$\left(H_0\psi\right)_x = \sum_{y\in\mathbb{Z}^D} \hat{t}_{x-y}\psi_y, \tag{2}$$

where ψ is a N-component spinor and $\hat{t}_a$s are $N\times N$ matrices with complex entries, such that $\hat{t}_{-a} = (\hat{t}_a)^\dagger$. Here, N represents the number of molecular orbitals per repeating cells. The Hamiltonian has the chiral-symmetry if there exists a unitary $N\times N$-matrix S with the properties:

$$S^2 = 1,\ S^\dagger = S,\ \text{and}\ SH_0S^{-1} = -H_0. \tag{3}$$

An immediate consequence of this symmetry is that the energy spectrum of the Hamiltonian is symmetric to the reflection relative to $E = 0$. The Fermi level is always fixed at $E = 0$ for systems with chiral-symmetry and since we are interested in insulators, we assume the existence of a spectral gap in the energy spectrum of H_0 at $E = 0$. This is possible only if N is even.

When translational symmetry is present, the model can be represented in the $\boldsymbol{k}$-space, where the dynamics is generated by the family of Bloch-Hamiltonians:

$$H(\boldsymbol{k}) : \mathbb{C}^N \to \mathbb{C}^N,\ \ H(\boldsymbol{k}) = \sum_a \hat{t}_a e^{\imath a\cdot\boldsymbol{k}}. \tag{4}$$

In this case, the chiral symmetry reads:

$$SH(\boldsymbol{k})S^{-1} = -H(\boldsymbol{k}). \tag{5}$$

One direct consequence of this symmetry is that the Hamiltonian takes the block-form[19]:

$$H(\boldsymbol{k}) = \begin{pmatrix} 0 & h(\boldsymbol{k}) \\ h(\boldsymbol{k})^\dagger & 0 \end{pmatrix} \tag{6}$$

if one works in the basis provided by the eigenvectors of S. The matrix h is invertible, in which case one can define a winding number:

$$\nu = \frac{-(\frac{1}{2}(D-1))!}{(2\pi i)^{\frac{D+1}{2}} D!} \int_{\mathbb{T}^D} \mathrm{Tr}\left\{\left(h(\boldsymbol{k})^{-1}\mathbf{d}h(\boldsymbol{k})\right)^D\right\} \in \mathbb{Z}, \tag{7}$$

over the Brillouin torus $\mathbb{T}^D$. One can use the homotopically equivalent flat-band version of the Hamiltonian:

$$\frac{H(\boldsymbol{k})}{|H(\boldsymbol{k})|} = \begin{pmatrix} 0 & q(\boldsymbol{k}) \\ q(\boldsymbol{k})^\dagger & 0 \end{pmatrix}, \tag{8}$$

and define the winding number as:

$$\nu = \frac{-(\frac{1}{2}(D-1))!}{(2\pi i)^{\frac{D+1}{2}} D!} \int_{\mathbb{T}^D} \mathrm{Tr}\left\{\left(q(\boldsymbol{k})^{-1}\mathbf{d}q(\boldsymbol{k})\right)^D\right\} \in \mathbb{Z}. \tag{9}$$

The advantage of the latter is that q is a unitary matrix, but many times Eq. 7 is easier to compute analytically.

The topological invariant can be formulated directly in the real-space representation [1]. Indeed, consider the flat-band Hamiltonian, which in the basis provided by the eigenvectors of S (this time viewed as an operator in real-space) takes the following block-form:

$$\frac{H_0}{|H_0|} = \begin{pmatrix} 0 & Q_0 \\ Q_0^\dagger & 0 \end{pmatrix}. \tag{10}$$

The Bloch-Floquet representation of Eq. 10 is nothing else but Eq. 8. Then the covariant real-space representation of the winding number can be obtained by applying the Bloch-Floquet transformation in reverse on Eq. 9 [1]:

$$\nu = \frac{(i\pi)^{\frac{D-1}{2}}}{D!!} \sum_{\rho \in S_D} (-1)^\rho \, \mathcal{T} \left\{ \prod_{j=1}^{D} Q_0^{-1} [X_{\rho_j}, Q_0] \right\}, \tag{11}$$

where $\mathcal{T}$ represents the trace per volume, $\boldsymbol{X} = (X_1, \ldots, X_D)$ denotes the position operator, $(X_j \boldsymbol{\psi})(\boldsymbol{x}) = x_j \boldsymbol{\psi}(\boldsymbol{x})$, and the summation is over all permutation of the indices. Since Eq. 11 is completely equivalent with Eqs. 7 and 9, the ν defined in Eq. 11 takes integer values, if evaluated in the idealistic limit of infinite volumes.

B. Homogeneous Disordered Lattice Models with Chiral-Symmetry

The generic disordered lattice Hamiltonians take the form:

$$(H_\omega \boldsymbol{\psi})_x = \sum_{y \in \mathbb{Z}^d} \hat{t}_{x,y}(\omega) \boldsymbol{\psi}_y, \tag{12}$$

where $\hat{t}_{x,y}(\omega)$ are $N \times N$ matrices with complex entries which depend on ω, a random variable from a probability space $\left(\Omega, d\boldsymbol{P}(\omega)\right)$ representing the disorder configurations. The system is said to be homogeneous if:

$$\hat{t}_{x-a,y-a}(\omega) = \hat{t}_{x,y}(\mathrm{t}_a \omega), \tag{13}$$

where t_a are probability-preserving, ergodic automorphisms on Ω, implementing the lattice-translations group. This is an important condition, because then the collection $\{H_\omega\}_{\omega \in \Omega}$ defines a covariant family of observables:

$$T_a H_\omega T_a^{-1} = H_{\mathrm{t}_a \omega}, \tag{14}$$

for any lattice translation T_a. The key point is that, if $F_\omega, G_\omega, \ldots$ are covariant observable, then, according to Birkhoff's ergodic theorem, the trace per volume is independent of the disorder configuration (with probability one) and is equal to an average over disorder:

$$\mathcal{T}\{F_\omega G_\omega \ldots\} = \int_\Omega d\omega \; \mathrm{tr}_{\mathbf{0}}\{F_\omega G_\omega \ldots\} \tag{15}$$

where $\mathrm{tr}_{\mathbf{0}}$ denotes the trace over the molecular orbitals in the first unit cell. Note that Eq. 15 states that any correlation function involving covariant observables is self-averaging. This is the principle behind the self-averaging of the non-commutative winding number.

A homogeneous disordered system is chiral symmetric if:

$$S H_\omega S^{-1} = -H_\omega \text{ for all } \omega \in \Omega. \tag{16}$$

Considering again the flat-band Hamiltonian and working in the basis provided by the eigenvectors of S:

$$\frac{H_\omega}{|H_\omega|} = \begin{pmatrix} 0 & Q_\omega \\ Q_\omega^\dagger & 0 \end{pmatrix} \tag{17}$$

with Q_ω a unitary operator. The natural generalization of the winding number is then:

$$\boxed{\nu = \frac{(i\pi)^{\frac{D-1}{2}}}{D!!} \sum_{\rho \in S_D} (-1)^\rho \, \mathcal{T} \left\{ \prod_{j=1}^{D} Q_\omega^{-1} [X_{\rho_j}, Q_\omega] \right\}}. \tag{18}$$

The righthand side can be easily seen to take finite values when the kernel of Q_ω decays exponential fast, as it is the case (on average) when the Fermi level resides in a region of localized spectrum. Based on our previous arguments, the non-commutative formula evidently has the self-averaging property. However, there is no a prior reason to think that the non-commutative winding number defined in Eq. 18 is integer when the spectral gap is closed. Nevertheless, if the Fermi level resides in a region of dynamical localization, this follows from the following index theorem proved in Ref. [18]:

Theorem [18]. Let $\sum_{j=1}^{D} X_j \sigma_j$ be the Dirac operator, where σ_i's are the D-generators of the odd Clifford algebra. Let Π denote the projector onto the positive spectrum of the Dirac operator and assume:

$$\int_\Omega d\omega \; |\langle \boldsymbol{x} | Q_\omega | \boldsymbol{y} \rangle| \leq A e^{-\gamma |\boldsymbol{x} - \boldsymbol{y}|}, \tag{19}$$

for some strictly positive A and γ. Then, with probability one in ω, $\Pi Q_\omega \Pi$ is a Fredholm operator and:

$$\nu = \text{Index } \Pi Q_\omega \Pi. \tag{20}$$

Furthermore, the Fredholm index on the right is independent of ω and is invariant against any continuous deformations of the Hamiltonian as long as Eq. 19 is satisfied.

Of course, Eq. 19 holds true if the Fermi level resides in a region of Anderson localized energy spectrum [18]. A direct prediction of the above result is the fact that ν can change only if the localization length diverges at $E = 0$. This was already confirmed numerically in Ref. [1] for the crossing $\nu = 0 \to \nu = 1$ in a model from AIII-symmetry class, and it will be further confirmed by our new numerical results in a broader setting.

C. Computing the Non-Commutative Winding Number

We now come to the important question of how to compute the non-commutative winding number. For this type of calculations, the following practical solution was devised in a series of works [11, 12, 17]. The most difficult part of the problem is how to represent or approximate the commutators $[X_j, Q_\omega]$ on a finite volume with periodic boundary conditions. On the infinite volume:

$$\langle x_j|[X_j, Q_\omega]|x'_j\rangle = (x_j - x'_j)\langle x_j|Q_\omega|x'_j\rangle, \tag{21}$$

and clearly the factor $x_j - x'_j$ is antagonistic to the periodic boundary conditions. But here is a set of key observations:

- The kernel $\langle x_j|Q_\omega|x'_j\rangle$ decays exponentially, on average, as $|x_j - x'_j|$ is increased.
- When restricting x_j to a finite domain $-N \leq x_j \leq N$ and imposing periodic boundary conditions, we are practically placing the system on the circle C_N of perimeter $2N + 1$.
- The factor $x_j - x'_j$ is antagonistic to this circle but we only need to represent it exactly for x_j close to x'_j, which leaves plenty of room to make it compatible with the circle (i.e. periodic).

Based on these guiding principles, the following procedure was proposed in Ref. [17]. Let $f : [-1, 1] \to \mathbb{R}$ be a smooth and periodic function such that $f(r) = r$, for $|r|$ smaller than some $\alpha \lesssim 1$. This function is used to define a function on the circle C_N: $f_N(x) = Nf(x/N)$, which has the correct periodicity and is equal to x for $|x| < \alpha N$. Let us consider its discrete Fourier representation:

$$f_N(x) = \frac{1}{2N+1}\sum_\lambda c_\lambda \lambda^x, \tag{22}$$

where the sum is over all $2N+1$ solutions of the equation $z^{2N+1} = 1$. This will enable us to extend the domain of this function indefinitely (note that $x_j - x'_j$ takes values in the interval $[-2N, 2N]$) and to finally define the proper replacement of the antagonistic factor in Eq. 21:

$$x_j - x'_j \to \sum_\lambda c_\lambda \lambda^{x_j - x'_j}. \tag{23}$$

From the above approximation, the approximated form of the commutators can be derived. Numerically, we found that the periodicity of the starting function f is not that important in practice, and in most of our calculations we simply use $f(r) = r$ over the entire $[-1, 1]$ interval. In this case, the Fourier coefficients are known explicitly and given below.

Summarizing, the canonical and optimal finite-volume approximation scheme that emerges from the above arguments consists of substituting the commutator $[X_j, Q_\omega]$ with:

$$\boxed{\lfloor X_j, \widetilde{Q}_\omega \rfloor = \sum_{\lambda\neq 1} c_\lambda \lambda^{X_j}\widetilde{Q}_\omega\lambda^{-X_j},\ \ c_\lambda = \frac{\lambda^{N+1}}{1-\lambda}.} \tag{24}$$

where $\widetilde{Q}_\omega$ represents the finite-volume approximation of Q_ω, obtained from the restriction $\widetilde{H}_\omega$ of H_ω on the finite volume. Based on the key factors listed above, Ref. [17] established the following rigorous result. Let Φ_j be smooth functions and let the accent $\sim$ indicate the restriction to a finite volume, then

$$\begin{aligned}&\Big|\mathcal{T}\{[X_{\alpha_1}, \Phi_1(H_\omega)][X_{\alpha_2}, \Phi_2(H_\omega)]\ldots\}\\ &-\widetilde{\mathcal{T}}\{\lfloor X_{\alpha_1}, \Phi_1(\widetilde{H}_\omega)\rfloor\lfloor X_{\alpha_2}, \Phi_2(\widetilde{H}_\omega)\rfloor\ldots\}\Big| < C_\Phi e^{-\beta N}\end{aligned} \tag{25}$$

where the constant C_Φ has an explicit expression in terms of the Φ_j functions. Based on this result, any correlation function involving localized observables and their commutators with the position operators can be canonically approximated on a finite volume, and this approximation converges exponentially fast to the thermodynamic limit. In particular, the canonical finite-volume approximation of the non-commutative winding number in arbitrary odd dimension D is:

$$\nu = \frac{(i\pi)^{\frac{D-1}{2}}}{D!!}\sum_{\rho\in S_D}(-1)^\rho\,\widetilde{\mathcal{T}}\left\{\prod_{j=1}^{D}\widetilde{Q}_\omega^{-1}\lfloor X_{\rho_j}, \widetilde{Q}_\omega\rfloor\right\}. \tag{26}$$

For convenience, we write the explicit expression in 1-dimension, which is used in the present numerical simulations:

$$\nu = \widetilde{\mathcal{T}}\left\{\widetilde{Q}_\omega^{-1}\lfloor X, \widetilde{Q}_\omega\rfloor\right\}. \tag{27}$$

In the regime of strong disorder, the quantization of the winding number obtained with this formula is typically exact up to six digits of precision.

III. MODELS AND PRELIMINARY ANALYSIS

We consider the following homogeneous disordered model from the AIII-symmetry class ($x \in \mathbb{Z}$):

$$\begin{aligned}(H\boldsymbol{\psi})_x = {}& m_x\,\hat{\sigma}_2\boldsymbol{\psi}_x\\ &+ {}^1\!/_2\,t_x[(\hat{\sigma}_1 + i\hat{\sigma}_2)\boldsymbol{\psi}_{x+1} + (\hat{\sigma}_1 - i\hat{\sigma}_2)\boldsymbol{\psi}_{x-1}]\\ &+ {}^1\!/_2\,t'[(\hat{\sigma}_1 + i\hat{\sigma}_2)\boldsymbol{\psi}_{x+2} + (\hat{\sigma}_1 - i\hat{\sigma}_2)\boldsymbol{\psi}_{x-2}],\end{aligned} \tag{28}$$

where $\hat{\sigma}$'s are Pauli's matrices. The disorder is present in the first-neighbor hopping and in the onsite potential:

$$t_x = t + W_1\omega_x,\ \ m_x = m + W_2\omega'_x,$$

where ω_x, ω'_x are independent randomly generated numbers, uniformly distributed in $[-0.5, 0.5]$. The

model in Eq. 28 preserves only the chiral symmetry $\hat{\sigma}_3 H \hat{\sigma}_3 = -H$, as the first term in Eq. 28 breaks both the particle-hole ($C = \sigma_3\mathcal{K}$) and time-reversal ($T = \mathcal{K}$, $\mathcal{K}$= complex conjugation) symmetries. The difference between this model and the one from the previous work [1] is the second-neighbor hopping term, which enables a richer phase diagram. We have also explored third-neighbor terms and obtained even richer phase diagrams, but those results are not reported here.

It is informative to discuss the phase diagram of the model in the absence of disorder ($W_{1,2} = 0$). In this case, the Bloch Hamiltonians take the form:

$$H(k) = \begin{pmatrix} 0 & t'e^{i2k} + te^{ik} - im \\ t'e^{-i2k} + te^{-ik} + im & 0 \end{pmatrix}, \quad (29)$$

which obeys $\sigma_3 H(k) \sigma_3^{-1} = -H(k)$. The winding number of the model can be analytically computed using Eq. 7:

$$\nu = \frac{1}{2\pi i} \oint_{|z|=1} dz \, \frac{2t'z + t}{t'z^2 + tz - im}, \;\; z = e^{ik}. \quad (30)$$

The poles of the integrand in the last line are located at:

$$z_{1,2} = \frac{-t \pm \sqrt{t^2 + 4imt'}}{2t'}, \quad (31)$$

and using the residue theorem, one can easily see that:

$$\nu = \begin{cases} 0 \text{ if both poles are outside the unit circle} \\ 1 \text{ if one pole is inside the unit circle} \\ 2 \text{ if both poles are inside the unit circle} \end{cases} \quad (32)$$

The key observation here is that, by fixing some parameters and varying the others, we can generate all phase transitions discussed in our introduction. Indeed, by fixing $t = 1$ and varying t' and m, we obtain the phase diagram shown in Fig. 1(a) where all three phases $\nu = 0, 1, 2$ can be seen. If we set $t = 0$, then both poles exit or enter the unit circle synchronously upon varying m, leading to the phase diagram shown in Fig. 2(a), where only the $\nu = 0$ and $\nu = 2$ phases can be seen.

By changing the Pauli matrix in the first term of Eq. 28, from $\hat{\sigma}_2$ to $\hat{\sigma}_1$, the symmetry class of the model becomes BDI type:

$$\begin{aligned} (H\boldsymbol{\psi})_x = {} & m_x \, \hat{\sigma}_1 \boldsymbol{\psi}_x \\ & + 1/2 \, t_x[(\hat{\sigma}_1 + i\hat{\sigma}_2)\boldsymbol{\psi}_{x+1} + (\hat{\sigma}_1 - i\hat{\sigma}_2)\boldsymbol{\psi}_{x-1}] \\ & + 1/2 \, t'[(\hat{\sigma}_1 + i\hat{\sigma}_2)\boldsymbol{\psi}_{x+2} + (\hat{\sigma}_1 - i\hat{\sigma}_2)\boldsymbol{\psi}_{x-2}], \end{aligned} \quad (33)$$

Indeed, besides the chiral symmetry, the above model also preserves the time-reversal and charge-conjugation symmetries. The time-reversal operation squares to one in this case.

In the absence of disorder ($W_{1,2} = 0$), the Bloch Hamiltonians take the form:

$$H(k) = \begin{pmatrix} 0 & t'e^{i2k} + te^{ik} + m \\ t'e^{-i2k} + te^{-ik} + m & 0 \end{pmatrix}, \quad (34)$$

which obeys $\sigma_3 H(k) \sigma_3^{-1} = -H(k)$. The winding number of the model can be again analytically computed using Eq. 7:

$$\nu = \frac{1}{2\pi i} \oint_{|z|=1} dz \, \frac{2t'z + t}{t'z^2 + tz + m}, \;\; z = e^{ik}. \quad (35)$$

The poles of the integrand in the last line are located at:

$$z_{1,2} = \frac{-t \pm \sqrt{t^2 - 4mt'}}{2t'}, \quad (36)$$

and using the residue theorem again, one can easily see that:

$$\nu = \begin{cases} 0 \text{ if both poles are outside the unit circle} \\ 1 \text{ if one pole is inside the unit circle} \\ 2 \text{ if both poles are inside the unit circle} \end{cases} \quad (37)$$

As such, by fixing some parameters and varying the others, we can generate all phase transitions discussed in our introduction. Indeed, by fixing $t = 1$ and varying t' and m we obtain the phase diagram shown in Fig. 1(d), where all three phases $\nu = 0, 1, 2$ can be seen. Furthermore, when m is increased, the square root in Eq. 36 becomes purely imaginary and both poles exit the unit circle synchronously upon increasing m, enabling us to witness a phase transition between $\nu = 0$ and $\nu = 2$. Furthermore, by fixing $t = 0$, we obtain the phase diagram shown in Fig. 2(c) where only the $\nu = 0$ and $\nu = 2$ phases can be seen.

In the presence of disorder, our tools of analysis are the non-commutative winding number already introduced and discussed above, and the dynamical localization length of the system. The latter is computed using the recursive transfer matrix [20, 21], as briefly explained here. Substituting Eqs. (28) and (33) into the Schrodinger equation $(H\boldsymbol{\psi})_x = E\boldsymbol{\psi}_x$, we can obtain:

$$\begin{aligned} \begin{pmatrix} \boldsymbol{\psi}_{x+2} \\ \boldsymbol{\psi}_{x+1} \end{pmatrix} &= \boldsymbol{T}_x \begin{pmatrix} \boldsymbol{\psi}_{x+1} \\ \boldsymbol{\psi}_x \end{pmatrix} \\ &= \begin{pmatrix} -\frac{\eta t_{x+1}}{m_{x+2}} & -\frac{\eta E t_x}{m_{x+2}} & \frac{\eta E^2}{m_{x+2}t'} - \frac{\eta t'}{m_{x+2}} & -\frac{\eta^2 E m_x}{m_{x+2}t'} \\ 0 & -\frac{t_x}{t'} & \frac{E}{t'} & -\frac{\eta m_x}{t'} \\ 1 & 0 & 0 & 0 \\ 0 & 1 & 0 & 0 \end{pmatrix} \begin{pmatrix} \boldsymbol{\psi}_{x+1} \\ \boldsymbol{\psi}_x \end{pmatrix}, \end{aligned} \quad (38)$$

where $\eta = 1/i$ correspond to the AIII and BDI symmetry classes, respectively. Due to the existence of the second neighboring hopping t' term, an analytic expression of the localization length at $E = 0$ cannot be obtained as like that in Ref. [1]. Here, the localization length Λ is computed numerically by:

$$\Lambda = \frac{1}{\gamma_{min}}, \quad (39)$$

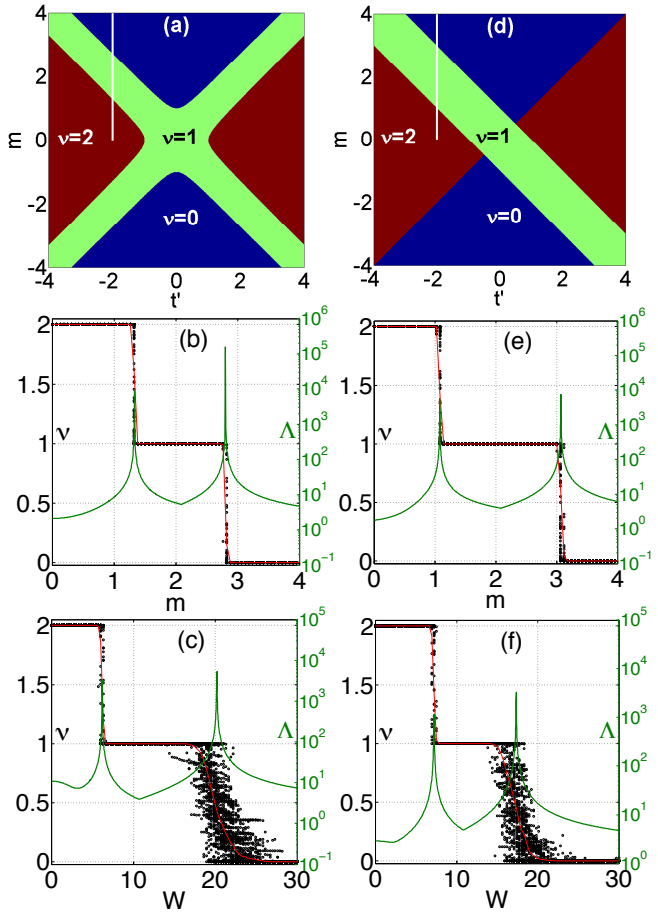

FIG. 1. (Color online) (a) and (d) The phase diagrams in the phase space (m, t') at $t = 1$ and $W_{1,2} = 0$. (b) and (e) Maps of the winding number Eq. 27 and of the localization length $\Lambda(E = 0)$ along the paths shown in the upper panels (see the light colored segments), with disorder fixed at $2W_1 = W_2 = 2$. (c) and (f) Maps of the winding number Eq. 27 and of the localization length $\Lambda(E = 0)$ as a function of disorder $W = 2W_1 = W_2$, at $t = 1$, $m = 1$ and $t' = -2$. The panels in the left column correspond to the AIII-symmetric model Eq. 28, and the ones in the right column to the BDI symmetric model Eq. 33. The scattered points represent the un-averaged output of Eq. 27 for 100 independent disorder configurations, and the solid (red) line represents the average. The computations for ν were done with a chain of $N = 1000$ unit cells, and in the computation of $\Lambda(E = 0)$ the transfer matrix was iterated 10^8 times.

where the smallest positive Lypunov exponent γ_{min} is defined by the eigenvalues $\{e^{\gamma_i}; i = 1 - 4\}$ of the matrix

$$\mathbf{\Gamma} = \lim_{N\to\infty}\left[\prod_{x=1}^{N} \boldsymbol{T}_x \prod_{x=N}^{1} \boldsymbol{T}_x^{\dagger}\right]^{1/2N}.$$

Note that the numerical method about how to obtain the smallest positive Lypunov exponent precisely can be found in Ref. [20, 21]. From Eq. (39), if the smallest positive Lypunov exponent γ_{min} is very close to 0 or $e^{\gamma_{min}} \sim 1$ there exists a delocalized state, which is indeed

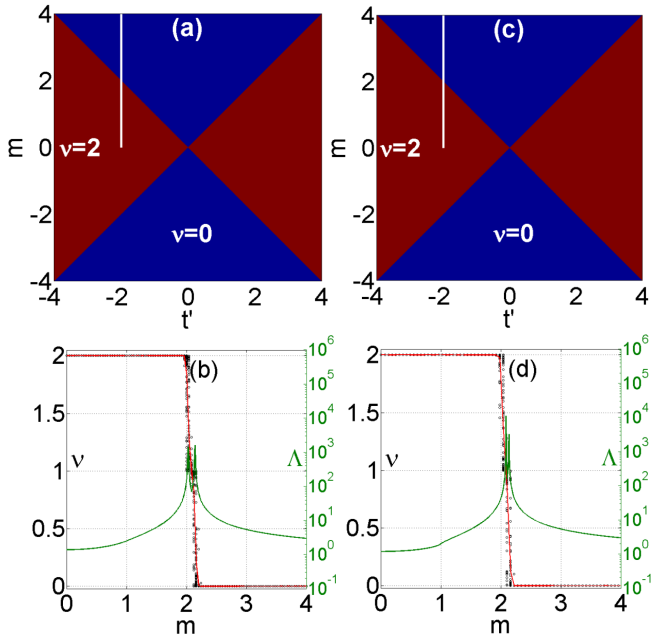

FIG. 2. (Color online) (a) and (c) The phase diagrams in the phase space (m, t') at $t = 0$ and $W_{1,2} = 0$. (b) and (d) Maps of the winding number Eq. 27 and of the localization length $\Lambda(E = 0)$ along the paths shown in the upper panels (see the light colored segments), with disorder fixed at $2W_1 = W_2 = 2$. Everything else is the same as in Fig. 1

observed at $E = 0$ at the phase transitions of the AIII and BDI symmetric systems.

IV. MAPPING ν AT STRONG DISORDER

We first turn on the disorder and keep it fixed at the levels $W_1 = 1$ and $W_2 = 2$ while mapping the non-commutative winding number along the paths shown in Fig. 1(a) and Fig. 1(d) for the AIII and BDI models, respectively. The level of disorder is strong enough to close the insulting gaps of the models throughout these paths. The results of the numerical calculations are shown in Fig. 1(b) and Fig. 1(e), which present the output of separate runs for 100 disorder configurations (the scattered data) and the average of ν over these disorder configurations (the red line). As one can see, the scattered data and the average overlap almost perfectly, which is a direct manifestation of the self-averaging property of the non-commutative formula. Furthermore, ν can be seen to take the cascade of strict quantized values 2, 1 and 0, for both symmetry classes, with very sharp transitions between the quantized values. The maps of the dynamical localization length along the same paths, shown on the same graphs, reveal Anderson localization-delocalization transitions at each step where ν changes its quantized value.

Next, we demonstrate that the same cascade of phase transitions can be driven by disorder. For this, we repeat

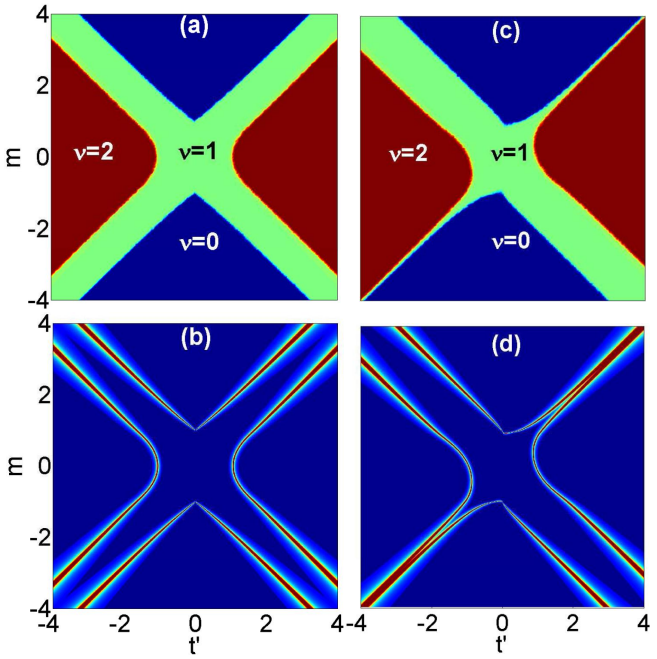

FIG. 3. The maps of the winding number (a) and (c) and localization length (b) and (c) as computed with Eqs. 26 and with the numerical transfer matrix method, respectively, by setting $t = 1$ and $W_1 = W_2 = 2$. The computations of ν were done for $N = 1000$ and averaged over 10 disorder configurations. The transfer matrix was iterated 10^8 times. Note that the figures in the left panel and in the right panel correspond to the class AIII model and the class BDI model, respectively.

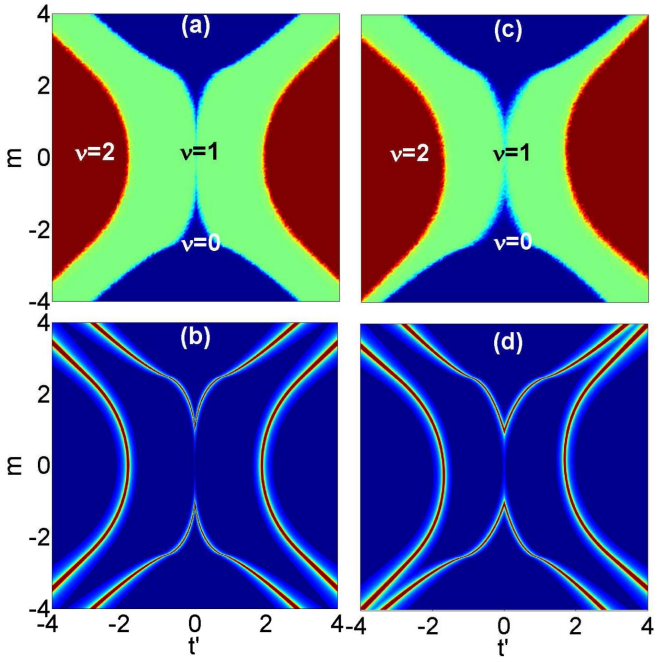

FIG. 4. Same as Fig. 3, except for $W_1 = W_2 = 5$.

the previous calculations but now we fix the model parameters at $t = 1, m = 1$ and $t' = -2$, which places the system deep in the $\nu = 2$ phase, and then we increase the disorder strength in the following fashion $W_2 = 2W_1 = W$, with W running from 0 to the extreme value of 30. The results are shown in Figs. 1(c) and 1(f) for the AIII and BDI symmetric models, respectively, and the cascade of transitions is clearly present. Here, again, the scattered data shows the output of ν for 100 independent runs with different disorder configurations, and the continuous (red) line represents the disorder average. The self-averaging property is clearly seen at work in these figures, except at the second topological phase transition, but those fluctuations are understandable given the extremely large value of disorder. The numerically calculated localization length can be seen again to diverge at the topological phase transitions.

The calculations so far show that the non-commutative winding number can take more than the values 0 and 1 in the presence of strong disorder. By considering third-neighbor hopping term we were able to generate topological phases with winding number 3 and this leaves little doubt that ν can take any integer value. We now investigate the transition from $\nu = 2$ directly into $\nu = 0$, and demonstrate that these two phases are distinct. For this, we set the parameter t to zero and we fix $t' = -2$ so that in the clean limit we obtain the phase diagrams shown in Figs. 2(a,c). It is important to remark that in this case there are hoppings only between odd sites, and separately between the even sites, hence we effectively have two disconnected chains. However, we introduce the same disorder as in panels (b,c) of Fig. 1, $2W_1 = W_2 = 2$, in which case the first-neighbor hoppings are restored and the chains become coupled through disorder. We map ν along the paths Γ_1' and Γ_2' and the results for the two models are shown in Figs. 2(b,d), together with a map of the dynamical localization length. The Anderson localization-delocalization is clearly visible, which is a strong indication that the $\nu = 2$ and $\nu = 0$ phases are indeed distinct.

Lastly, we have combed the energy spectrum and found that the dynamical localization length is always finite, except at the Anderson localization-delocalization phase transitions discussed above. This shows that for both AIII and BDI systems, the quantized topological invariant is carried entirely by localized states.

V. ANALYSIS OF THE PHASE DIAGRAMS

Our analysis continues with computations of the phase diagrams, which will reveal that the phases characterized by different ν's are entirely disconnected from each other and that they are separated by an Anderson localization-delocalization transition. Furthermore, the phase diagrams for both models display an intricate behavior as a functions of disorder. The phase boundaries move non-monotonically with the disorder, with the domain of the non-trivial topological phases increasing at

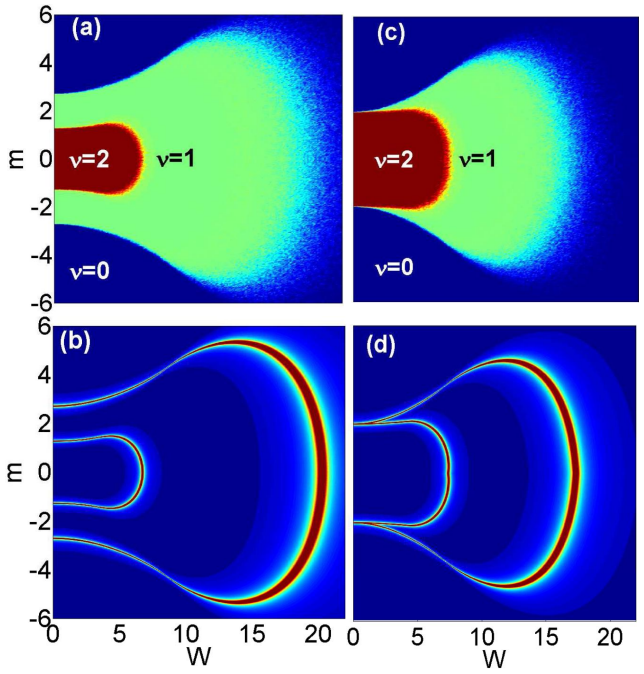

FIG. 5. The maps of the winding number (a) and (c) and localization length (b) and (d) as computed with Eqs. 26 and with the numerical transfer matrix method, respectively, by setting $t = 1$, $t' = 2$ and $W = 2W_1 = W_2$. The computations of ν were done for $N = 1000$ and averaged over 10 disorder configurations. The transfer matrix was iterated 10^8 times. Note that the figures in the left panel and in the right panel correspond to the class AIII model and the class BDI model, respectively.

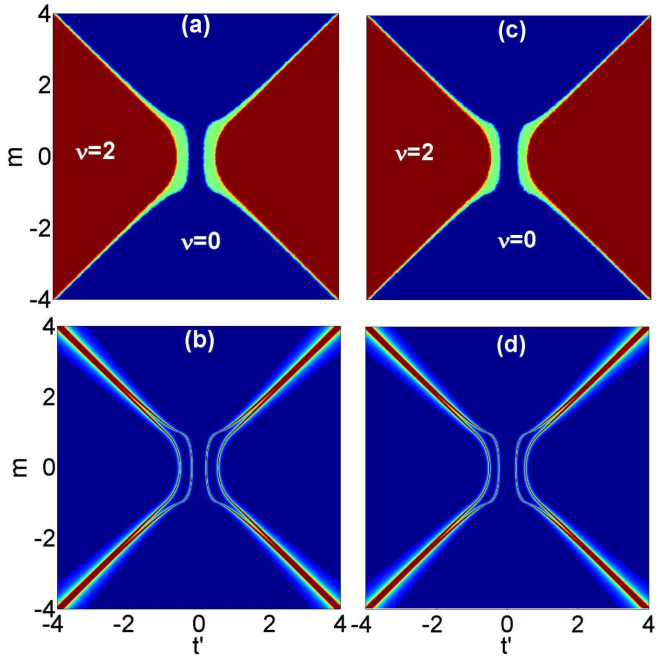

FIG. 6. The maps of the winding number (a) and (c) and localization length (b) and (d) as computed with Eqs. 26 and with the numerical transfer matrix method, respectively, by setting $t = 1$, $t' = 2$ and $2W_1 = W_2 = 2$. The computations of ν were done for $N = 1000$ and averaged over 10 disorder configurations. The transfer matrix was iterated 10^8 times. Note that the figures in the left panel and in the right panel correspond to the class AIII model and the class BDI model, respectively.

the beginning and then decreasing until the domains disappear. In the process, the so called Anderson topological insulator phase emerges [22–24].

The phase diagrams of the models in the (t', m) plane and at a finite disorder $W_1 = W_2 = 2$ are shown in Fig. 3. Specifically, the maps of the non-commutative winding number are reported in panel (a) for the AIII model and in panel (c) for the BDI model. Comparing the first map with the one obtained at zero disorder, one can immediately observe a relative stability of the phases, but when comparing the second map an instability can be witnessed in panel (c), caused by the spill of phase $\nu = 1$ in between the phases $\nu = 0$ and $\nu = 2$. This is interesting because it shows that the disorder alone can transform the $2 \to 0$ transition (which is very interesting by itself) into the monotonic sequence of transitions $2 \to 1 \to 0$. Panels (b) and (d) report the maps of the localization length $\Lambda(E = 0)$, showing fine lines where $\Lambda(E = 0)$ diverges and which coincide perfectly (within the numerical accuracy) with the boundaries between different ν-phases. This confirms that the topological phases (identified by the values of ν) are separated by an Anderson localization-delocalization transition throughout the phase boundaries. We have repeated the calculations with a stronger disorder $W_1 = W_2 = 5$ and the results are reported in Fig. 4. Here one can see that the phase diagrams have been distorted quite pronouncedly by the disorder, and the protrusion of $\nu = 1$ phase in between the $\nu = 1, 2$ phases has been accentuated. In fact, the phase diagrams for the two models look very alike, which is expected because in the regime of infinite disorder the two models are similar. The maps of the dynamical localization length at $E = 0$ show again that all the topological phases are separated from each other by an Anderson localization-delocalization transition.

The phase diagrams in the (W, m) plane, with $W = 2W_1 = W_2$, are shown in Fig. 5. Here one can explicitly see the topological phases growing as the disorder is turned on, and as a result the topological domain with $\nu = 1$ spills into the domain formerly occupied by the trivial phase, and the domain with $\nu = 2$ spills into the domain formerly occupied by the $\nu = 1$ phase. For example, hypothetical materials described by the two models with $m = 3$, would be trivial in the clean limit but become topological insulators when increasing the disorder, as shown in panels 4(a) and 4(c). Furthermore, for the BDI model, the phase $\nu = 1$ is entirely absent in the clean limit, but it robustly emerges after the disorder is turned on and fully develops at extreme values of disorder. The maps of the dynamical localization length continues to

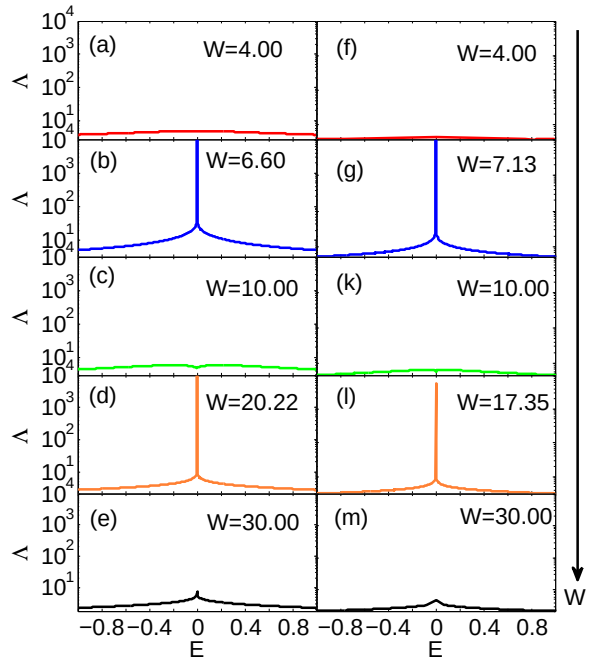

FIG. 7. Maps of the localization length as a function of energy, for five points of the phase diagram reported in Fig. 5(a) and Fig. 5(c), all taken at $t = 1$, $t' = -2$ and $m = 0.5$. The level of disorder is indicated on each panel. The left and right panels correspond to the class AIII model and the class BDI model, respectively.

show that all topological phases are separated by an Anderson localization-delocalization transition.

Next, we have considered the phase diagrams from Fig. 2, which are for the clean limit and show only the phases $\nu = 2$ and $\nu = 0$, and we introduced a disorder $2W_1 = W_2 = 2$. The phase diagram in the plane (m, t') and in the presence of this disorder is reported in Fig. 6. Here we see again the phase $\nu = 1$ emerging again between the $\nu = 0$ and $\nu = 2$ two phases, even if it was not there to start with. It becomes clearer now that the transition $\nu = 2 \to \nu = 0$ is not stable and instead it seems that this transition is always broken to the cascade of transitions $\nu = 2 \to \nu = 1 \to \nu = 0$ when the disorder is introduced. Nevertheless, if $\nu = 0$ and $\nu = 2$ were identical phases, then inherently we would have encountered many instances where a crossing from $\nu = 2$ into $\nu = 0$ happens without an Anderson localization-delocalization transition. However, from the maps of the dynamical localization length reported in the lower panels of Fig. 6, one can see that an Anderson transition is always encountered when crossing from $\nu = 0$ phase to $\nu = 2$ phase and viceversa. This leaves very little doubt that these two phases are indeed distinct.

Lastly, in Fig. 7 we report traces of the dynamical localization length as a function of energy, taken at five points of the phase diagrams reported in Fig. 5. The first, third and fifth points are located inside the $\nu = 2$, $\nu = 1$ and $\nu = 0$ phases, respectively, while the second and fourth points are located on the phase boundary between the $\nu = 2$ and $\nu = 1$ phases, and between the $\nu = 1$ and $\nu = 0$ phases, respectively. The computations were performed for the AIII (right panel) as well as the BDI (left panel) models. The important observation here is that, for all points that are away from the phase boundary, the localization length is finite, proving the absence of the extended states in the spectrum, even for the topological phases topological phases. This is a direct confirmation that the topological winding number is carried entirely by localized states. Furthermore, one can see that the divergence of the localization length at the boundary between the phases develops strictly at $E = 0$, and no trace of the so called levitation and annihilation phenomenon can be detected.

VI. CONCLUSIONS

The non-commutative winding numbers for 1-dimensional disordered phases from the AIII and BDI symmetry classes have been explicitly shown to take several integer values, and that a phase characterized by a specific value of the winding number is enclosed in a phase-boundary where an Anderson localization-delocalization transition takes place. In particular, the phases characterized by $\nu = 0$ and $\nu = 2$ have been shown to be distinct, a fact that rules out a $\mathbb{Z}_2$-classification and supports a $\mathbb{Z}$-classification for these systems. This also shows that the electric polarization, which takes the quantized values 0 and $\frac{1}{2}$, does not provide a full classification for these phases.

We have also demonstrated explicitly that the energy spectra of the topological phases are fully localized, the topological invariants are carried entirely by localized states, and as a consequence, the Anderson localization-delocalization transition develops entirely from this localized spectrum, without the well known mechanism of pair levitation and annihilation.

The numerical algorithms for the non-commutative winding number and their performance was discussed in detail. In all our simulated phase diagrams, the quantization of the topological invariant in the presence of extreme disorder was accurate to more than six digits of precision. The self-averaging property, which was also explicitly demonstrated, makes the non-commutative winding number one of the most effective tools for the analysis of topological systems with chiral symmetry.

ACKNOWLEDGMENTS

We would like to thank Ian Mondragon-Shem and Taylor L. Hughes for insightful discussions. This work was supported by the U.S. NSF grants DMS-1066045, DMR-1056168, NSFC under grants No. 11204065 and NSF-Hebei Province under grants No. A2013205168.

[1] I. Mondragon-Shem, J. Song, T. L. Hughes, and E. Prodan, arXiv:1311.5233 (2013).
[2] A. P. Schnyder, S. Ryu, A. Furusaki, and A.W.W. Ludwig, Phys. Rev. B **78**, 195125 (2008).
[3] S. Ryu, A. P. Schnyder, A. Furusaki, and A. W. Ludwig, New J. Phys. **12**, 065010 (2010).
[4] R. D. King-Smith and D. Vanderbilt, Phys. Rev. B **47**, 1651(R) (1993).
[5] R. Resta, Rev. Mod. Phys. **66**, 899 (1994).
[6] G. Ortiz and R. M. Martin, Phys. Rev. B **49**, 14202 (1994).
[7] X.-L. Qi, T. L. Hughes, and S.-C. Zhang, Phys. Rev. B **78**, 195424 (2008).
[8] T. Hughes, E. Prodan, and B. A. Bernevig, Phys. Rev. B **83**, 245132 (2011).
[9] A. M. Turner, Y. Zhang, R. S. K. Mong, and A.Vishwanath, Phys. Rev. B **85**, 165120 (2012).
[10] M. Onoda, Y. Avishai, and N. Nagaosa, Phys. Rev. Lett. **98**, 076802 (2007).
[11] E. Prodan, T. Hughes, and B. Bernevig, Phys. Rev. Lett. **105**, 115501 (2010).
[12] E. Prodan, J. Phys. A: Math. Theor. **44**, 113001 (2011).
[13] Z. Xu, L. Sheng, D. Y. Xing, E. Prodan, and D. N. Sheng, Phys. Rev. B **85**, 075115 (2012).
[14] M. J. Gilbert, B. A. Bernevig, and T. L. Hughes, Phys. Rev. B **86**, 041401 (2012).
[15] B. Leung and E. Prodan, Phys. Rev. B **85**, 205136 (2012).
[16] B. I. Halperin, Phys. Rev. B **25**, 2185 (1982).
[17] E. Prodan, Appl. Math. Res. eXpress **2013**, 176 (2013).
[18] E. Prodan and H. Schulz-Baldes, arXiv:1402.5002 (2014).
[19] A. P. Schnyder, S. Ryu, and A. W. W. Ludwig, Phys. Rev. Lett. **102**, 196804 (2009).
[20] A. MacKinnon and B. Kramer, Phys. Rev. Lett. **47**, 1546 (1981).
[21] A. MacKinnon and B. Kramer, Z. Phys. B **53**, 1 (1983).
[22] J. Li, R. L. Chu, J. K. Jain, and S. Q. Shen, Phys. Rev. Lett. **102**, 136806 (2009).
[23] C. W. Groth, M. Wimmer, A. R. Akhmerov, J. Tworzydlo, and C.W. J. Beenakker, Phys. Rev. Lett. **103**, 196805 (2009).
[24] E. Prodan, Phys. Rev. B **83**, 235115 (2011).